GEOPHYSICS, VOL. 68, NO. 4 (JULY-AUGUST 2003); P. 1150–1160, 11 FIGS.
10.1190/1.1598107

Fracture characterization at Valhall: Application of P-wave amplitude variation with offset and azimuth (AVOA) analysis to a 3D ocean-bottom data set

Stephen A. Hall* and J-Michael Kendall‡

ABSTRACT

The delineation and characterization of fracturing is important in the successful exploitation of many hydrocarbon reservoirs. Such fracturing often occurs in preferentially aligned sets; if the fractures are of subseismic scale, this may result in seismic anisotropy. Thus, measurements of anisotropy from seismic data may be used to delineate fracture patterns and investigate their properties. Here fracture-induced anisotropy is investigated in the Valhall field, which lies in the Norwegian sector of the North Sea. This field is a chalk reservoir with good porosity but variable permeability, where fractures may significantly impact production, e.g., during waterflooding. To investigate the nature of fracturing in this reservoir, P-wave amplitude variation with offset and azimuth (AVOA) is analyzed in a 3D ocean-bottom cable (OBC) data set. In general, 3D ocean-bottom seismic (OBS) acquisition leads to patchy coverage in offset and azimuth, and this must be addressed when considering such data. To overcome this challenge and others associated with 3D OBS acquisition, a new method for processing and analysis is presented. For example, a surface fitting approach, which involves analyzing azimuthal variations in AVO gradients, is used to estimate the orientation and magnitude of the fracture-induced anisotropy. This approach is also more widely applicable to offset-azimuth analysis of other attributes (e.g., traveltimes) and any data set where there has been true 3D data acquisition, land or marine. Using this new methodology, we derive high-resolution maps of P-wave anisotropy from the AVOA analysis for the top-chalk reflection at Valhall. These anisotropy maps show coherent but laterally varying trends. Synthetic AVOA modeling, using effective medium models, indicates that if this anisotropy is from aligned fracturing, the fractures are likely liquid filled with small aspect ratios and the fracture density must be high. Furthermore, we show that the fracture-normal direction is parallel to the direction of most positive AVO gradient. In other situations the reverse can be true, i.e., the fracture-normal direction can be parallel to the direction of the most negative AVO gradient. Effective medium modeling or comparisons with anisotropy estimates from other approaches (e.g., azimuthal variations in velocity) must therefore be used to resolve this ambiguity. The inferred fracture orientations and anisotropy magnitudes show a degree of correlation with the positions and alignments of larger scale faults, which are estimated from 3D coherency analysis. Overall, this work demonstrates that significant insight may be gained into the alignment and character of fracturing and the stress field variations throughout a field using this high-resolution AVOA method.

INTRODUCTION

The Valhall field, situated in the Norwegian North Sea, is an Upper Cretaceous chalk reservoir discovered in 1975 and produced since 1982. Unfortunately, the high potential of the reservoir in the form of significant oil-filled porosity (reaching 50% in some areas) is offset by poor matrix permeabilities. However, permeabilities up to an order of magnitude higher than those measured in cores have been detected in production analysis (Ali and Alcock, 1994). This enhanced permeability has been attributed to fractures, and it has been suggested that such fracturing could be exploited to improve production. Additionally, azimuthal anisotropy has been observed in dipole sonic data from the producing chalk horizon (Mueller

Presented at the 70 Annual International Meeting, Society of Exploration Geophysicists. Manuscript received by the Editor May 31, 2001; revised manuscript received November 21, 2002.
*Formerly University of Leeds, School of Earth Sciences, Leeds, United Kingdom; presently Heriot-Watt University, Institute of Petroleum Engineering, Edinburgh EH14 4AS, United Kingdom. E-mail: steve.hall@pet.hw.ac.uk.
‡University of Leeds, School of Earth Sciences, Woodhouse Lane, Leeds LS2 9JT, United Kingdom. E-mail: m.kendall@earth.leeds.ac.uk.
© 2003 Society of Exploration Geophysicists. All rights reserved.

et al., 1997); it may be induced by aligned fracturing. Thus, mapping this anisotropy throughout the reservoir could allow characterization of fracturing and its spatial distribution plus the identification of compartmentalization and an assessment of directional permeability. Such information may be used to guide directional drilling or water injection and to assess potential infill targets in the reservoir.

The fracture-induced anisotropy observed in the dipole–sonic data may be observable using surface seismic techniques, such as observations of amplitude variation with offset and azimuth (AVOA) (e.g., Thomsen, 1988; Lynn and Thomsen, 1990; Lynn et al., 1996; Mallick et al., 1998; Macbeth et al., 1999; Gray et al., 2002; Holmes and Thomsen, 2002). In a marine setting, 3D ocean-bottom seismic (OBS) acquisition provides the multiazimuth data necessary for reservoir-wide AVOA studies; such data are available at Valhall. We apply a new approach for processing 3D OBS data for P-wave AVOA analysis at Valhall to provide maps of azimuthal anisotropy in the reservoir. These maps are thus interpreted to provide a spatially dependent characterization of fracturing in the reservoir.

The basics of AVOA and fracture-induced azimuthal anisotropy are presented first, followed by a brief description of the geology of the area and acquisition of the data. A methodology for processing such 3D OBS data for AVOA analysis is outlined, addressing some of the processing challenges encountered. [These issues are discussed in more detail by Hall (2000), where the approach is formulated.] Application of the methodology and AVOA analysis at Valhall is subsequently presented. Effective medium modeling constrains the interpretation, leading to the final fracture orientation maps and insight into the likely fracture properties.

FRACTURES, AZIMUTHAL ANISOTROPY AND AVOA

Aligned subseismic-scale fracturing can produce seismic anisotropy (i.e., seismic velocity varies with direction) and leads to measurable directional differences in traveltimes and reflectivity. If the fractures are vertically aligned, they will produce azimuthal anisotropy (the simplest case being horizontal transverse isotropy, or HTI) such that reflectivity of an interface depends on azimuth as well as offset.

Exact reflection and transmission coefficients for plane waves at a boundary between two isotropic half-spaces are provided in Aki and Richards (1980). However, the reflectivity is commonly approximated for purposes of data analysis, e.g., for the P-P reflection amplitude R_{pp} between isotropic media:

$$R_{pp}(i) = A + B\sin^2 i + C\sin^2 i\tan^2 i \qquad (1)$$

for an incidence phase angle i. The terms A, B, and C are defined by Chapman (1976).

If either of the media bounding the interface is azimuthally anisotropic, the AVO will have an azimuthal dependence. Rüger (1998) and Vavryčuk and Pšenčík (1998) extend the basic AVO approximation (1) to provide analytical equations describing AVOA in media with a single fracture alignment. Thus, for HTI media, R_{pp} is given as a function of the incident and azimuthal phase angles, i and ϕ, respectively:

$$R_{pp}(i,\phi) = A + [B + D\cos 2\phi]\sin^2 i + [C + E\cos 2\phi + F\cos 4\phi]\sin^2 i\tan^2 i, \qquad (2)$$

where A, B, C, D, E, and F are functions of the contrasts in velocity and azimuthal anisotropy parameters across the reflecting interface (see Appendix A). Equation (2) shows that the AVO in azimuthally anisotropic media will vary azimuthally as functions of $\cos 2\phi$ and $\cos 4\phi$. (For symmetries more complex than HTI, there maybe additional, higher order terms in $\cos\phi$.) For small incidence angles (i.e., short offsets) the $\sin^2 i\tan^2 i$ term will be small; therefore, in many cases the $\cos 2\phi$ (elliptical) azimuthal component will dominate and the AVOA can be simplified to an elliptical form. [The tradeoff between the $\cos 2\phi$ and $\cos 4\phi$ terms is discussed further in Hall and Kendall (2000).] Near-offsets are typically defined as angles of incidence less than about 25°–30°, but this is situation dependent and must be assessed through modeling or data observation. Furthermore, the assumption of a $\cos 2\phi$ azimuthal dependence should be verified in the data prior to imposing this constraint in any analysis.

Ideally, AVOA analysis involves fitting a surface to the amplitude data such that the AVO trend and azimuth dependence are solved simultaneously. However, in equation (2), ϕ is the azimuth of the measurement relative to the fracture normal but this alignment is unknown and a more general form is desired which is not dependent on prior knowledge of this parameter. Grechka and Tsvankin (1998) provide a general equation to describe an elliptical variation in NMO velocity when the orientations of the major axes of the ellipse are unknown. This is adapted here to give a similar expression for an elliptical variation in the near-offset AVO gradient [B in equation (1)]. Thus, with an elliptical variation in the near-offset AVO gradient term, the AVOA is described by

$$R_{pp}(i,\phi')_{near} = A + \left(b_{11}\cos^2\phi' + 2b_{12}\cos\phi'\sin\phi' + b_{22}\sin^2\phi'\right)\sin^2 i + O(\sin^2 i\tan^2 i), \qquad (3)$$

where ϕ' is the azimuth from some arbitrary coordinate system (in this study, the data acquisition grid) and the long-offset term is a function of higher order cosine terms. The terms b_{ij} are coefficients describing the general form of an ellipse whose orientation and magnitude are given by

$$\varphi = \tan^{-1}\left[\frac{b_{22} - b_{11} + \left((b_{22}-b_{11})^2 + 4b_{12}^2\right)^{\frac{1}{2}}}{2b_{12}}\right], \qquad (4)$$

$$\zeta_{1,2} = \frac{1}{2}\left[b_{11} + b_{22} \pm \left((b_{11}-b_{22})^2 + 4b_{12}^2\right)^{\frac{1}{2}}\right] \qquad (5)$$

(after Grechka and Tsvankin, 1998). The angle φ defines the rotation of the principal axes of the AVO gradient ellipse ζ_1 and ζ_2 ($\zeta_1 > \zeta_2$) from the arbitrary coordinate system.

GEOLOGIC CONTEXT

The reservoirs of interest at Valhall lie within a typical North Sea sequence as indicated in Figure 1. The overall structure forms a shallow anticline (see Figure 2) but is relatively flat over the range imaged by a common midpoint (CMP) gather (dips are generally <10° for the top chalk; over the main area of interest in this study, they are much less and thus negligible). Figure 1 also indicates the main geological units and the primary reservoirs: the Tor Formation (Cretaceous chalk, about 24 m average thickness) and the lower Hod (Cretaceous chalk, about 30 m thick). The Lista Formation forms the roof

rock (Paleocene shales about 20 m thick on average). The main target for this study is the top of the hard chalk horizon, which appears as a sharp jump in the P-wave and shear-wave velocities with a slight increase in density. Therefore, this event is easily identified in seismic sections.

Large-scale faulting exists in the chalk unit, which continues into the underlying layers but does not extend far into the relatively simple geology of the overburden. Figure 2 shows this horizon in map view; the faulting is primarily related to the doming of the structure (these faults were mapped from offset reflections in the 3D streamer data). Two main orthogonal fault orientations exist in the area; they are approximately northwest–southeast and southwest–northeast. Smaller scale fracturing is thought to be associated with these large faults and could provide significant directional permeability within the fault-bounded compartments. If aligned these small fractures may result in seismic anisotropy.

THE VALHALL 3D-4C OBC DATA SET

The Valhall 3D-4C ocean-bottom cable (OBC) data were acquired by Geco-Prakla (Rosland et al., 1999) using orthogonal source and receiver lines with a geometry as shown in Figure 3. The acquisition involved ocean-bottom cables deployed at 600 m spacing containing receiver groups at 25-m intervals along their 6000-m length. Each receiver group consisted of seven, four-component receivers (see Figure 3c). The patch shooting, over pairs of receiver lines (Figure 3b), used an air-gun source at about 7.5 m depth with 25 m in-line spacing and 600 m line spacing.

This OBC acquisition design would be expected to provide an ideal data distribution for azimuthal analyses with a wide sampling of both offset and azimuth. Figure 4d shows the offset-azimuth distribution for data in a 75 × 75-m CMP bin, indicating the data are grouped into discrete offset-azimuth patches. Therefore, the offset-azimuth coverage is not ideal for single subsurface bins. Furthermore, the data distribution varies throughout the survey such that, for example, some CMPs have no very short-offset data. This patchy and spatially varying data distribution will have an impact on any azimuthal analysis. Such issues also have a more general significance for processing such

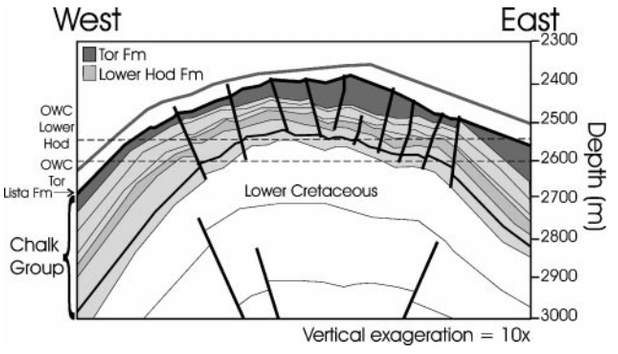

FIG. 1. Schematic cross-section through the region, indicating the main geological features. The primary reservoirs are in the Tor Formation and the Lower Hod, and the oil–water contacts (OWC) for each are indicated. The Lista Formation forms the roof rock. Large-scale faulting is indicated as subvertical black lines, and this is concentrated in the chalk group. The main horizon of interest in this study is the top of the chalk. (Figure provided by BP.)

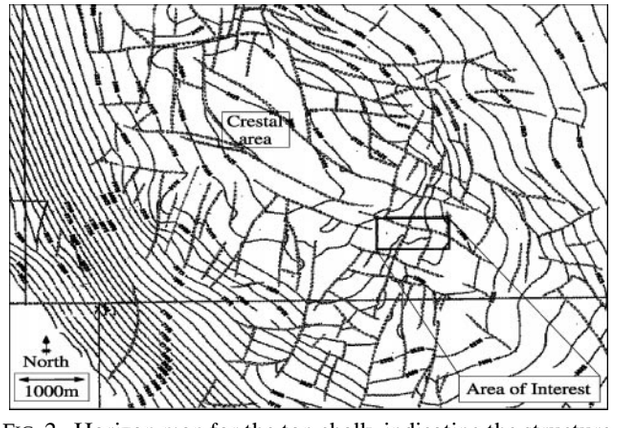

FIG. 2. Horizon map for the top chalk, indicating the structure (contours, solid black lines have a 25-m interval; the crest of the structure is highlighted) and major faulting (double dashed lines). The area considered in the analysis is also indicated.

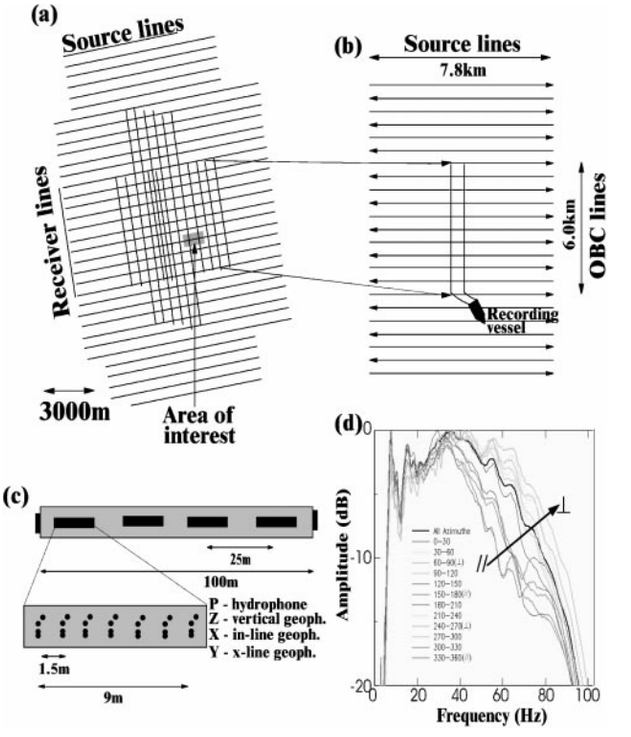

FIG. 3. Acquisition design for this OBC data example. (a) Orthogonal source- and receiver-line layout with 600-m spacing between each line. (b) Data acquired using patch shooting involving twenty-three, 7.8-km lines at 600 m spacing with shots every 25 m over pairs of receiver lines. (c) Receiver arrays positioned at 25 m along each 6-km receiver cable with seven, four-component sensors at 1.5 m spacing in each group. The area of interest for the anisotropy analysis is highlighted in (a). (d) Amplitude spectra for different azimuths bins (produced by Dave Wilson, BP, 1999); the receiver line parallel (//) direction is approximately 350°/170°. Above about 35 Hz, there is significant variation in the frequency content along the different azimuths. This is from a previously applied summation of the seven receivers in each array providing an azimuth-dependent array filter that cuts out more of the higher frequencies in the direction parallel to the array than perpendicular to it.

data (e.g., velocity analysis and gather flattening, so even the stacked sections may be affected). These processing challenges are discussed in Hall (2000), where the new approach for azimuthal analysis of 3D OBS data is formulated.

APPROACH FOR AVOA DATA

As discussed, AVOA processing of 3D OBS data must be able to account for patchy offset-azimuth distribution (Figure 4d). Thus, common-offset or azimuth techniques used in previous works (e.g., Lynn et al., 1996; Mallick et al., 1998; Macbeth et al., 1999) are inappropriate for these data, so a surface-fitting approach is taken in this work. Based on the observations made in Hall (2000) and insight gained in previous work (Hall and Kendall, 2000), a new processing flow for azimuthal analysis of horizon amplitudes from 3D OBC CMP data has been developed (Hall, 2000). Figure 4 outlines this processing flow, which aims to avoid the creation or loss of azimuthal characteristics and automate the procedure as much as possible. This methodology could be applied to any data set where there is 3D acquisition, land or marine—particularly where there is a patchy offset-azimuth distribution but still sufficient offset-azimuth content in CMP gathers. Note that only the vertical components of the 4C data are utilized in this work, although converted phases (P-S) also hold valuable information (Hall and Kendall, 2000). The preprocessing and AVOA analysis are discussed in more detail below.

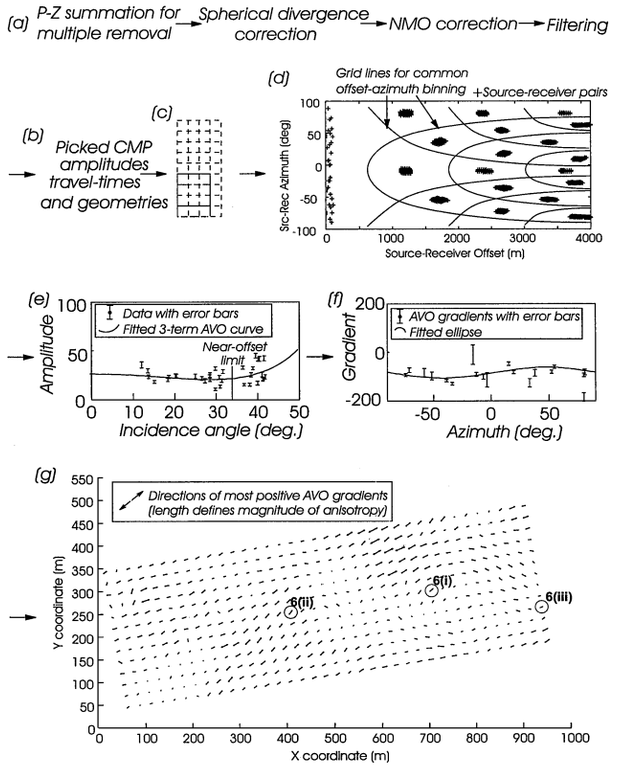

FIG. 4. Schematic representation of the processing flow for AVOA analysis of 3D OBS data. (a) Standard preprocessing to improve the primary reflections. (b) Amplitudes and traveltimes are picked in the CMP gathers and labelled with the CMP geometry data. (c) These amplitude and time data are regrouped into overlapping 75 × 75-m CMP gathers and binned to common offset-azimuth groups with offset and azimuth positions also averaged (d). (e) A 2D, Shuey-type AVO curve is fitted to the amplitude data to define the normal incidence amplitude and near-offset range. (f) These values are used to define the azimuthal variation in the near-offset AVO gradients for each of the 75 × 75-m data gathers. The gradients will have an elliptical variation with azimuth so an anisotropy ellipse can be determined. (g) The major axes of the near-offset AVO gradient ellipse for each CMP are plotted in map form to provide insight into fracture orientations and their spatial variability. The CMP locations of the AVOA data examples of Figure 6(i)–(iii) are also indicated. Note that a similar approach is applied for traveltimes but using NMO velocity rather than AVO gradient.

Initial data preparation

Prior to AVOA analysis, preprocessing should be minimized to reduce the risk of destroying or creating azimuthal variations in the data. However, to identify primary events, some preprocessing is inevitable. For these data P-Z summation, for multiple removal, and a spherical divergence correction are applied by Petroleum Geo-Services (PGS). In addition, the data are sorted into 25 × 25-m CMP bins; early, direct and refracted, arrivals are muted, NMO corrections are made, and a band-pass filter is applied (corner frequencies = 7, 14, 30, and 50 Hz). A relatively narrow band-pass filter cuts out azimuthal variations that exist at higher frequencies because of a previously applied summation of the seven-receiver arrays at each station that acts as an azimuth-dependent array filter (see Figure 3d). Three horizons are picked at about 1640 ms (base Miocene with maximum negative amplitude picked), at about 2630 ms (top chalk with maximum positive amplitude picked), and at another consistent event near 2130 ms (maximum positive amplitude picked) (see Figure 5).

AVOA analysis

After the amplitude, traveltime and geometry data of each event are extracted from the CMP gathers, the data are resorted, and the AVOA analysis is applied to the individual horizons using overlapping 75 × 75-m bins with a 25-m step. This

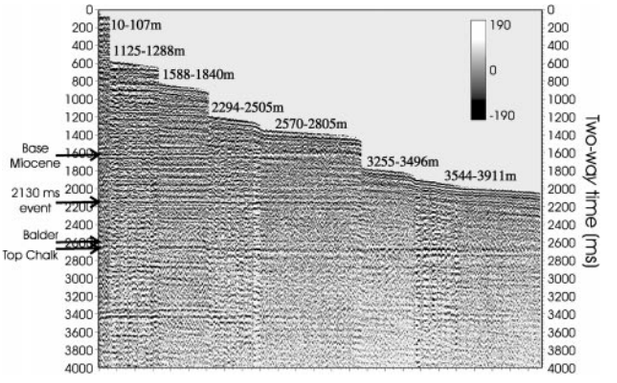

FIG. 5. An example of a flattened 75 × 75-m CMP gather. The offset ranges of the gather are indicated above the data; note the large, irregular gaps (see also the offset-azimuth distribution shown in Figure 4d). The three events picked in the later analysis plus the Balder are highlighted for reference. No static corrections have been applied, which may account for some of the jitter in the events (see Hall, 2000).

provides a measure of the azimuthal anisotropy at the center of each bin to yield a 25 × 25-m grid of anisotropy estimates with some spatial smoothing. An improved S/N ratio and averaging out of random shot–shot variations (e.g., in source magnitude and noise), without loss of the offset-azimuth quality, are achieved by exploiting the inherent redundancy of data. The data are naturally grouped into offset-azimuth patches (Figure 4d), because of the acquisition design, so each of these offset-azimuth groups in the 75 × 75-m gathers is binned to a single point where all attributes are averaged (including the offset and azimuth positions). This offset-azimuth binning also quantifies the scatter in the data, which is used to define the uncertainty bounds in the AVOA analysis (Figures 4e,f and 6). Furthermore, by mapping all of the data into the 0°–180° azimuth range, reciprocal source and receiver pairs are combined, which should remove some of the influence of source directivity.

Following the preprocessing and binning described above, AVOA analysis is applied using a surface fitting approach to the near-offset data only. It is assumed that the azimuthal trend in AVO for these data is elliptical. Thus, it is straightforward to solve for the AVO and azimuth dependence simultaneously by fitting an AVOA surface [equation (3)]. Inspection of the data (Figure 6b) shows that this is a valid assumption and the azimuthal variation in the near-offset AVO follows such a $\cos 2\phi$ trend [although the longer offsets may show more complicated trends; see equation (2)]. The axes of this near-offset elliptic trend will be aligned with the principal axes of the anisotropy and can thus provide insight into fracture orientations. Unfortunately, for these data the near-offset AVOA surface was poorly defined because of the irregular offset-azimuth sampling. Therefore, in this approach the AVOA analysis is applied in two stages to stabilize the result.

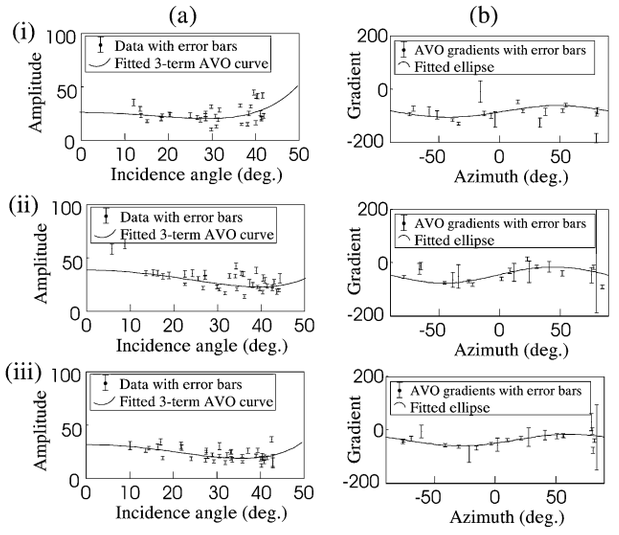

FIG. 6. (a) Examples of the amplitude data with error bars (quantified from the scatter in the data for each offset-azimuth bin and the best-fit 2D, Shuey-type AVO curves). (b) The corresponding near-offset AVO gradients for each of the data points [determined from the normal incidence amplitude derived using (a)] with the fitted azimuth ellipse plotted as a function of azimuth. The three examples are from CMPs at different positions in the acquisition grid, as indicated in Figure 4.

The first stage in the analysis uses all data points in each overlapping bin of CMPs to define a three-term AVO curve as described by equation (1) (see Figures 4e and 6a). This defines the normal incidence amplitude and the range over which the near-offset approximation is valid [i.e., where the azimuth-independent AVO can be described by just the terms A and B, in equation (1), and the azimuthal variation is thought to be approximately elliptical]. Utilizing the longer offset data at this stage stabilizes the estimation of the normal incidence term. The second step utilizes this normal incidence amplitude A as a priori information for the inversion of equation (3) to determine b_{ij} based on the assumption that the azimuthal variation in the near-offset AVO gradient is elliptical. The orientation and magnitude of any anisotropy can therefore be determined using equations (4) and (5) (see Figures 4f and 6b). Any influence from the $\sin^2 i \tan^2 i$ term can be accounted for by including the derived value for C [equation (1)] to provide a long-offset (azimuthally isotropic) weighting that reduces the error in the resultant anisotropy orientation estimates.

Following the approach outlined above, a measurement of the direction and magnitude of ζ_1, the most positive AVO gradient, is determined for the center of each of the overlapping 75 × 75-m CMP bins. These values can be plotted as vectors on a map, as in Figure 7. The magnitudes of these vectors are determined by the difference between the major and minor axes of the AVO gradient ellipse divided by the rms average of the two axes. The rms average is used to avoid division by zero or near-zero values. This nonzero scaling allows a direct comparison of different CMPs and different events (although the vectors shown are scaled to the maximum amplitude in the respective plot). For the remainder of this work, this scaled difference of the lengths of the ellipse axes is referred to as the magnitude of the near-offset AVO gradient anisotropy. This is not the same as the percentage velocity anisotropy, which is commonly used to define percentage anisotropy.

RESULTS AND INTERPRETATION

The three horizons defined earlier are analyzed over the small area of the survey indicated in Figures 2 and 3a. This area is about 975 × 450 m and contains 481 (25 × 25 m) CMP bins. This region was selected for analysis because it covers two intersections of source and receiver lines, allowing comparisons to be made between data which are imaged by equivalent parts of the acquisition grid (see Figure 3). Furthermore, this location avoids known data-quality problems related to shallow gas in the crestal area, and structural dips are minor.

The initial aim was to assess the success of the azimuthal analysis of AVO and traveltimes by looking for the following:

1) no evidence of the acquisition geometry in the anisotropy maps (the presence of this would indicate that the variations in AVO and velocities were caused by acquisition artifacts and not fracture-induced anisotropy);
2) different patterns of anisotropy in the different horizons (since the larger faulting does not extend far above the chalk, the upper horizons are expected to show different fracture patterns);
3) smooth spatial variations since a completely random variation in the orientation of the anisotropy vectors could indicate the suggested patterns in AVOA or velocities are not related to fracturing or anisotropy.

Once these constraints are satisfied, the results may be interpreted in terms of fracture characteristics, which may be compared with the known geology (e.g., large-scale fault patterns).

Figure 7 shows that the AVO anisotropy variations are not random, do not mirror the acquisition geometry, and show different trends for each horizon. Therefore, the initial goals have been satisfied; the next step is to interpret the observed trends. Since production is from the chalk horizon, the remainder of this section concentrates on the top-chalk reflection.

Top-chalk AVOA interpretation

Figure 7c is a map of the magnitude of the AVOA and the orientation of the major axes of the AVO gradient ellipses for a small area of the top-chalk reflector. Smooth spatial trends are observed in the anisotropy, varying over the entire area of interest. From these trends we can define discrete regions with different orientations and magnitudes of anisotropy. These may relate to areas of different fracture characteristics and correspond to fault-bounded compartments. For example, the northeast corner of the map shows a smooth rotation of the vectors from roughly southwest–northeast around to about northwest–southeast, flanked by distinct boundaries suggesting possible fault positions. Figure 7c also shows the magnitude of the near-offset AVO gradient anisotropy for the top chalk, highlighting the presence of northwest–southeast-trending structures.

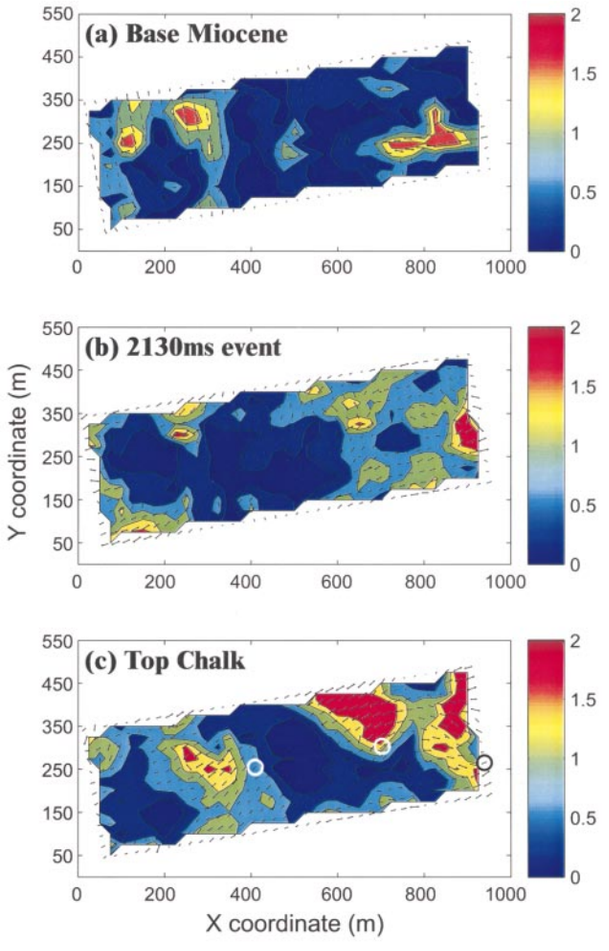

FIG. 7. Maps of the AVO anisotropy results for the three horizons of interest, indicated in Figure 5, over the area indicated in Figures 2 and 3. The vectors indicate the direction of the most positive AVO gradient; the length is the relative magnitude of the azimuthal variation in the AVO gradient scaled with respect to the maximum value at each horizon. The anisotropy magnitudes indicated by the colors are directly comparable between the different horizons. The positions of the source and receiver lines relative to these maps are indicated in Figure 3a. The CMP locations indicated in Figure 4 for the AVOA data examples of Figure 6 are highlighted by circles.

Unfortunately, the interpretation of AVOA is highly dependent on the fracture properties. Even the determination of fracture orientation may be ambiguous since the coefficient of $\cos 2\phi$ in equation (2) may be positive or negative (see Hall and Kendall, 2000). Therefore, additional constraints are needed to determine the true orientation of the fracturing with respect to the AVOA trends. To gain increased insight into the potential ambiguity in the interpretation, the following section presents a series of forward models and provides comparisons of synthetic and observed AVOA to help constrain some of the unknown fracture properties.

Constraints on the interpretation of AVOA from effective medium modeling

To constrain the interpretation of the AVOA data in terms of fracture properties (particularly orientation), an effective medium approach is used to model the expected azimuthal variation in AVO. A single alignment of fracturing is modelled with velocity and density data from local wells, using the so-called EFFECT approach [see Appendix B and Hall and Kendall (2000)]. Saturated brine-filled fractures and a gas-fill model indicate the end members. If the fractures contain oil, the results are assumed to lie between these two models. Examples are first provided for the AVO along different azimuths to the fracturing for brine- and gas-filled fractures (Figure 8). This is followed by examples of modelled amplitude versus azimuth for different incidence angles and varying aspect ratio (Figure 9). These two figures highlight some of the ambiguities that can exist in AVOA interpretation. [For a more detailed study, see Hall and Kendall (2000).] Subsequently, the same forward modeling approach is used to create a series of fracture scenarios and expected AVOA signatures that are compared to the AVOA data and thus provide constraints on the fracture interpretation.

Figure 8 shows synthetic AVO at different azimuths for the top-chalk reflection using a model with $v_p = 2141$ m/s, $v_s = 500$ m/s, and $\rho = 2240$ kg/m^3 in the overburden and $v_p = 3134$ m/s, $v_s = 1534$ m/s, and $\rho = 2300$ kg/m^3 in the chalk. These values are determined from log data, and we see that the modelled AVO is similar to the observed trends in the data (Figure 6). These figures also show that, for the offset range used in the AVOA analysis (around 0°–30°) with a brine fracture fill, the most positive near-offset AVO gradient is in the fracture normal direction. However, for gas-filled fractures (all other parameters the same) the most positive near-offset AVO gradient is along the fracture strike. These two examples clearly indicate that ambiguity can exist in the AVOA interpretation such that the fracture orientation inferred from the AVOA, and thus whether the vectors plotted in Figure 7c are the fracture

strike or fracture normal directions, can depend on the fracture fill. Extending this modeling to produce expected AVOA signatures for a range of fracture aspect ratios highlights another key parameter that defines the shape of the AVOA surface. Figure 9 shows that if the fractures are brine filled, the anisotropy orientations determined from the data (the direction of most positive near-offset AVO gradient) are likely to be the fracture normal direction for low aspect-ratio fractures (<0.05). However, if the fractures are gas filled, only at very low aspect ratio (<0.00025) will the orientations observed in the data be the fracture-normal direction. Furthermore, at longer offsets the $\cos 4\phi$ term becomes important and is also highly dependent on aspect ratio and fracture fill.

To provide constraints on the interpretation of the AVOA data, the expected AVOA anisotropy magnitude and polarity are calculated for a range of fracture scenarios using the modeling approach outlined above. Figure 10 presents these quantified AVOA magnitudes for the different fracture scenarios: gas or brine saturation, varying aspect ratio, varying crack density, and varying degree of equant porosity ϕ_p. This last parameter accounts for communication of fluid from the fractures to matrix porosity as described, for example, in Thomsen (1995). Figure 10 also shows a comparison of the synthetic and observed anisotropies to provide constraints on the model.

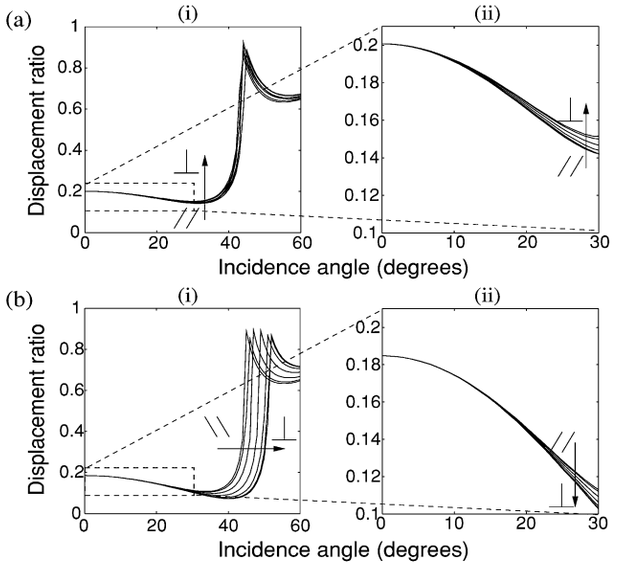

FIG. 8. (a) Modelled P-P AVO for the top-chalk reflection for 15° azimuth increments from the fracture strike direction to the fracture normal direction, as indicated by the arrows (amplitudes are given as the displacement ratio, which is the ratio of the incident to reflected wave displacements). (a) Brine-filled fractures and (b) gas-filled fractures with a crack density of 0.1 and a fracture aspect ratio of 0.001. (i) AVO for 0°–60° angles of incidence, showing the P-P critical reflection as a large amplitude peak from 40°–50°. (ii) Enlarged view of the AVO for the range 0°–30°, showing the change in AVO with azimuth over the near-offset range considered in the data analysis. For this model with a brine fracture fill, the most positive near-offset AVO gradient is in the fracture normal direction. For gas-filled fractures, the most positive near-offset AVO gradient is along the fracture strike. Also, the long-offset azimuthal variation in AVO is greater for gas-filled fractures; at shorter offsets, the opposite is observed.

This comparison indicates that to achieve the higher levels of anisotropy seen in the data (Figure 7c) it would be necessary to have a large crack density (around 0.1) of very thin fractures and a fracture fill that is more likely liquid than gas. Gas-filled fractures would have to be very thin (aspect ratio $\ll 0.001$) to provide the observed levels of anisotropy. This modeling also indicates that any communication of fluid to the matrix pore space will be minimal (i.e., $\phi_p \ll 0.1$). The most important observation from Figure 10 is that the observed levels of anisotropy are only possible if the maximum near-offset AVO gradient is perpendicular to the fracturing. Therefore, the maps of anisotropy shown previously for the top-chalk horizon actually indicate the fracture-normal directions. Based on this modeling, the revised predicted fracture map for the area of interest is shown in Figure 11.

Determining fault patterns from 3D coherency analysis

The fracturing inferred from the AVOA analysis may be related to the larger scale faulting. Therefore, the patterns seen in the AVOA maps may correlate with the positions and orientations of large-scale faults. Figure 2 provides some insight into the large-scale faulting, but a more detailed map of fault patterns may be derived from 3D coherency analysis of the stacked data.

Coherency analysis with 3D data is described by Bahorich and Farmer (1995) as a method for calculating the localized waveform similarity in both in-line and cross-line directions. Segments of seismic traces that intersect fault planes show different seismic character to adjacent segments, leading to distinct loss of trace-to-trace coherence. Therefore, faults appear as lines of low coherence that can be used to create fault maps.

Coherency analysis along a time slice through the stacked data at about 2670 ms (close to the level of the top-chalk reflection) is interpreted to provide a map of faulting in the chalk over the area of interest in the AVOA analysis. Figure 11 compares the AVOA results with the interpreted faults from the coherency analysis. Some correlation between spatial variation in fracture alignment, interpreted from the AVOA, and fault trace is observed. In addition, comparison of the magnitude of the anisotropy (Figure 7c) and the fault positions indicates that the northwest–southeast-trending faults appear to have more influence on the fracture pattern with a greater degree of fracturing associated with these faults. This suggests that the direction of maximum extension is southwest–northeast. In many places the AVOA-defined fracture pattern also appears to follow the time contours such that the fracturing is perpendicular to the maximum curvature of the horizon.

CONCLUSIONS

An approach for analyzing the azimuthal variations in P-wave AVO with a high spatial resolution has been applied to a 3D OBC data set. This approach could be applied to any data set, land or marine, where there is true 3D multiazimuth acquisition. Challenges involved in processing sparsely distributed OBC data have also been highlighted, indicating the difficulties caused by large spacings between source and receiver lines; this is discussed further by Hall (2000). In particular, a patchy

offset-azimuth distribution exists which must be considered in AVOA analysis of such data, so a surface-fitting approach is used instead of common-offset or-azimuth approaches described in earlier work. The approach used here is also applicable to offset-azimuth analysis of other attributes such as traveltimes.

The results from the AVOA analysis have been used to infer fracture orientations and compartmentalization in a small area of the data set. Insight into the nature of the anisotropy and fracturing has been gained through synthetic AVOA modeling using effective medium models to constrain the highlighted ambiguities in the AVOA interpretation. This modeling indicates that if the anisotropy is induced by aligned fractures, there must be a high density of fractures with low aspect ratios which are likely liquid filled and the fracture-normal direction is parallel to the direction of most positive AVO gradient. Thus, a map of the orientation and magnitude of fracturing derived from the AVOA data shows compartmentalization into areas of different fracture characteristics. Comparison of the inferred fracturing with an interpretation of faulting from 3D coherency analysis indicates a degree of correlation with larger scale faulting. Furthermore, the main north–northwest fracture orientation and secondary east–northeast trend are similar to those observed by Caley et al. (2001) in shear-wave splitting of microseismic data. Additionally, Granger et al. (2000) have consider horizontal component amplitude ratios of converted waves in the same OBC data and have found an orientation consistent with our results.

Future work in this area and with this data set must primarily involve refining the processing and inversion procedures with greater constraints from known rock and fracture properties to increase confidence in the results. In particular, the interpretation is highly sensitive to the fracture fill, so this parameter should be constrained first. Furthermore, refined forward modeling and improved fault determination are also necessary in addition to gaining a better understanding of the interrelationship of fractures and faulting. The long-offset P-P AVOA may provide additional information about the fracturing (see Figure 9). The P-S AVOA could also be used for this type of analysis (Hall and Kendall, 2000) and should provide independent, but complementary, data that will further constrain the fracture characterization.

ACKNOWLEDGMENTS

The authors acknowledge the advice and support of Olav Barkved (BPAmoco Norge) and colleagues at BP in Houston, especially Mike Mueller, Leon Thomsen, Gerry Beaudoin and Dave Wilson, where S.H. was an intern for the start of this work. We also thank BP Amoco Norge AS and the Valhall Partners, Amerada-Hess Norge A/S, Elf Petroleum Norge A.S., and Enterprise Oil Norge Ltd., for their support of this work and allowing it to be published. We would also like to acknowledge the input from the referees. Finally, we thank Joel Starr of PGS for bringing to our attention U.S. Patent 6 026 059 that relates to some of the phenomena discussed in this work, the existence of which we were not aware until just prior to publication.

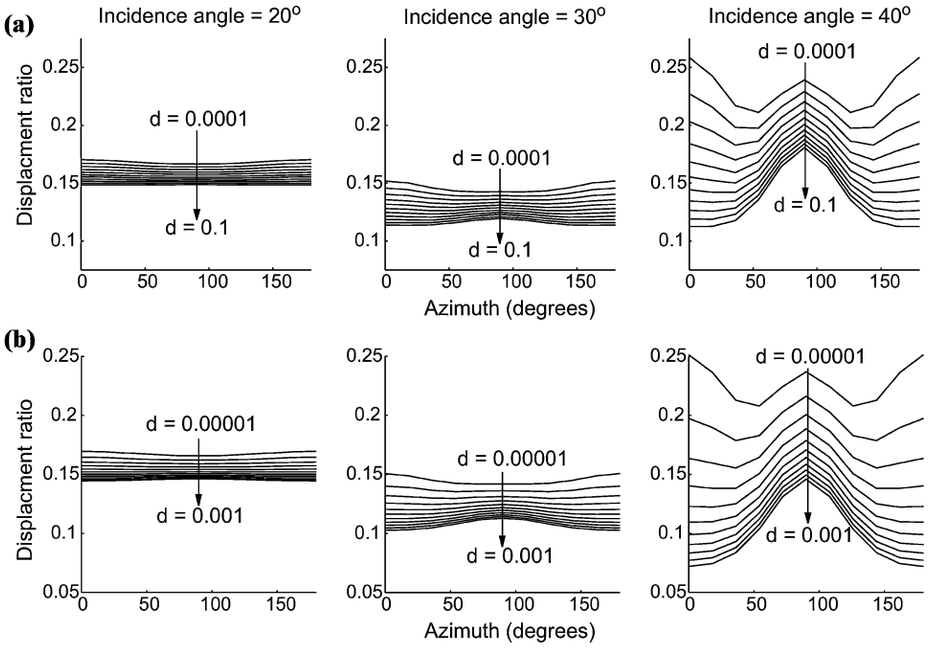

FIG. 9. Modelled P-P AVA for different incidence angles and varying aspect ratio d (amplitudes are given as the displacement ratio, which is the ratio of the incident to reflected-wave displacements). Crack density is 0.1 with (a) a brine fill and aspect ratio increasing linearly from 0.0001 to 0.1, as indicated by the arrows, and (b) a gas fill with aspect ratio increasing linearly from 0.00001 to 0.001, as indicated by the arrows. Although the amplitude data being considered in the azimuthal analysis only extends to about 30° incidence angle, the longer offset data (which is acquired but not used for the AVOA analysis) may contain significant information that could be used to further characterize the fracturing. Furthermore, for low aspect ratio fractures and at near-offsets, the reflection amplitude will have a positive $\cos 2\phi$ variation with azimuth from the fracture normal. However, for gas-filled fractures this only occurs with very low aspect ratio (around 0.00025 compared to about 0.05 for brine-filled fractures).

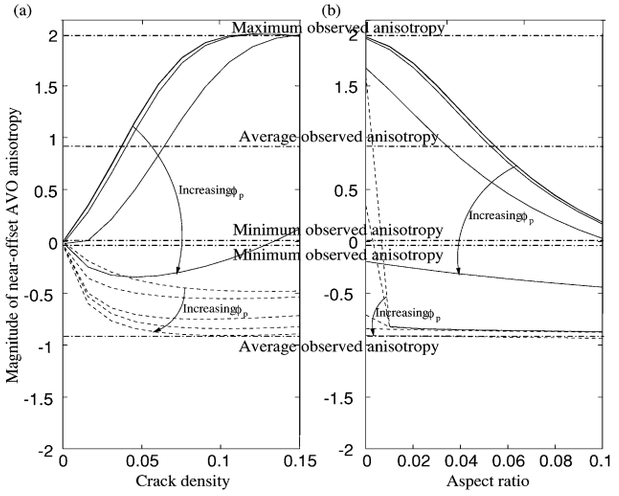

FIG. 10. Magnitude of modelled near-offset AVO-gradient anisotropy for different fracture models. Dashed lines are for gas-filled fractures; solid lines are for brine-filled fractures. The anisotropy magnitude is plotted against (a) increasing crack density, with an aspect ratio of 0.001, and (b) increasing aspect ratio, with a crack density of 0.1, for different values of equant porosity; $\phi_p = 0.0, 0.0001, 0.001, 0.01, 0.1$, with the arrow indicating the direction of increase. The alignment of most positive AVO gradient is in the fracture-normal direction for a positive anisotropy and in the fracture strike direction for a negative anisotropy. The observed anisotropies in the data (the minimum and average values are indicated and the maximum observed anisotropy is about 2.0) may be positive or negative since the orientation of the fracturing is undefined. However, since it is only possible to achieve the levels of anisotropy observed in the data when there is a positive anisotropy, this figure suggests that the anisotropy vectors in Figure 7c indicate the fracture normal directions.

REFERENCES

Aki, K., and Richards, P. G., 1980, Quantitative seismology: Theory and methods: W. H. Freeman & Co.

Ali, N., and Alcock, T., 1994, Valhall field—The first 10 years, *in* North Sea oil and gas reservoirs III: Kluwer Academic Publishers, 25–40.

Bahorich, M., and Farmer, S., 1995, 3D seismic discontinuity for faults and stratigraphic features: The coherency cube: The Leading Edge, **14**, 1053–1058.

Caley, A. J., Kendall, J-M., Jones, R. H., Barkved, O. I., and Folstad, P. G., 2001, Mapping fractures in 4D using microseismic data: 63rd Ann. Mtg., Eur. Assn. Expl. Geophys., Expanded Abstracts, Session F-23.

Chapman, C. H., 1976, Exact and approximate generalized ray theory in vertically inhomogeneous media: Geophys. J. Roy. Astr. Soc., **46**, 201–233.

Granger, P., Rollet, A., and Bonnot, J., 2000, Preliminary evaluation of azimuthal anisotropy over the Valhall field using C-wave data, *in* Anisotropy 2000: Fractures, converted waves, and case studies: Soc. Expl. Geophys., 772–775.

Gray, D., Roberts, G., and Head, K., 2002, Recent advances in determination of fracture strike and crack density from P-wave seismic data: The Leading Edge, **21**, 280–285.

Grechka, V., and Tsvankin, I., 1998, 3-D description of normal moveout in anisotropic inhomogeneous media: Geophysics, **63**, 1079–1092.

Hall, S. A., 2000, Rock fracture characterisation and seismic anisotropy: Application to ocean bottom seismic data: Ph.D. thesis, Univ. Leeds.

Hall, S. A., and Kendall, J-M., 2000, Constraining the interpretation of AVOA for fracture characterisation, *in* Anisotropy 2000: Fractures, converted waves, and case studies: Soc. Expl. Geophys., 107–144.

Holmes, G., and Thomsen, L., 2002, Seismic fracture detection at a Middle East offshore carbonate field: Soc. Petr. Eng. J., 78507.

Lynn, H. B., and Thomsen, L., 1990, Reflection shear-wave data collected near the principal axes of azimuthal anisotropy: Geophysics, **55**, 147–156.

Lynn, H. B., Simon, K. M., Bates, C., and Van Dok, R., 1996, Azimuthal anisotropy in P-wave (multiazimuth) data: The Leading Edge, **15**, 923–928.

Macbeth, C., Jakubowicz, H., Kirk, W., Li, X.-Y., and Ohlsen, F., 1999, Fracture-related amplitude variations with offset and azimuth in marine seismic data: First Break, **17**, 13–26.

Mallick, S., Craft, K. L., Meister, L. J., and Chambers, R. E., 1998, Determination of the principal directions of azimuthal anisotropy from P-wave seismic data: Geophysics, **63**, 692–706.

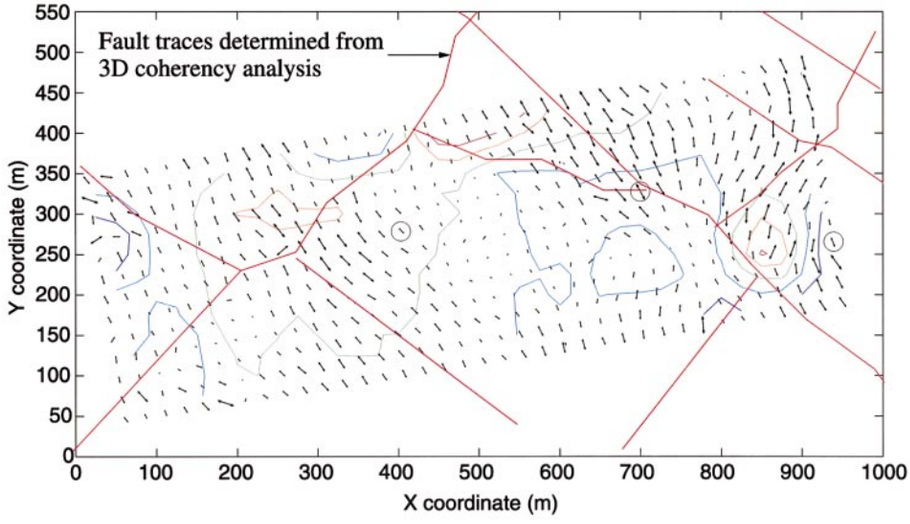

FIG. 11. Fracture pattern map for top-chalk horizon compared to interpreted fault traces from coherency analysis. The fracture orientations are derived from the near-offset AVO gradient anisotropy analysis. Based on the synthetic modeling summarized in Figure 10, the vectors shown are rotated by 90° from those in Figure 7c. Some correlation of the inferred fracture patterns and the large-scale faulting can be seen with a greater alignment of the fractures near the northwest–southeast-trending faults. In the southeast corner, the fracturing also appears to be perpendicular to the surface curvature defined by the time contours. The time contours are at 20-ms intervals, with red indicating deeper areas and dark blue shallower areas. The CMP locations highlighted by circles are those indicated in Figure 4 for the AVOA data examples of Figure 6.

Mueller, M. C., Barkved, O. I., and Thomsen, L. A., 1997, Dipole sonic results (Valhall area)—Implications for AVO and OBS interpretation: 59th Ann. Mtg., Eur. Assn. Expl. Geophys., Expanded Abstracts, Paper E050.
Rosland, B., Tree, E. L., and Kristiansen, P., 1999, Acquisition of 3D/4C OBS data at Valhall: 61st Ann. Mtg., Eur. Assn. Expl. Geophys., Expanded Abstracts, Paper 6017.
Rüger, A., 1998, Variation of P-wave reflectivity with offset and azimuth in anisotropic media: Geophysics, **63**, 935–947.
Schoenberg, M., and Sayers, C. M., 1995, Seismic anisotropy of fractured rock: Geophysics, **60**, 204–211.
Thomsen, L., 1988, Reflection seismology over azimuthally anisotropic media: Geophysics, **53**, 304–313.
——— 1995, Elastic anisotropy due to aligned cracks in porous rock: Geophys. Prosp., **43**, 805–829.
Vavryčuk, V., and Pšenčík, I., 1998, PP-wave reflection coefficients in weakly anisotropic elastic media: Geophysics, **63**, 2129–2141.

APPENDIX A

AVOA COEFFICIENTS FOR HTI MEDIA

The coefficients in equation (2), adapted from Rüger (1998), are

$$
\begin{aligned}
A &= \frac{1}{2}\frac{\Delta Z}{\bar{Z}},\\
B &= \frac{1}{2}\left[\frac{\Delta\alpha}{\bar{\alpha}} - \left(\frac{2\bar{\beta}}{\bar{\alpha}}\right)^2\frac{\Delta G}{\bar{G}} + \Delta\delta^{(v)} + 2\left(\frac{2\bar{\beta}}{\bar{\alpha}}\right)^2\Delta\gamma\right],\\
C &= \frac{1}{2}\frac{\Delta\alpha}{\bar{\alpha}} + \frac{1}{8}\left(3\Delta\epsilon^{(v)} + 2\Delta\delta^{(v)}\right),\\
D &= \frac{1}{2}\left[\Delta\delta^{(v)} + 2\left(\frac{2\bar{\beta}}{\bar{\alpha}}\right)^2\Delta\gamma\right],\\
E &= \frac{1}{2}\Delta\epsilon^{(v)},\\
F &= \frac{1}{8}\left[\Delta\epsilon^{(v)} - 2\Delta\delta^{(v)}\right].
\end{aligned}
\tag{A-1}
$$

Here, $Z = \rho\alpha$ is the vertical P-wave impedance and $G = \rho\beta^2$ is the vertical shear modulus where α, β, and ρ are, respectively, the vertical P-wave velocity, the vertical shear-wave velocity, polarized parallel to the fracture plane, and the density. The symbol Δ indicates differential values, for example, $\Delta\alpha = \alpha_2 - \alpha_1$, and the overscored terms are the average values, e.g., $\bar{\alpha} = \frac{1}{2}(\alpha_2 + \alpha_1)$, where the subscripts 1 and 2 indicate the properties of the upper and lower bounding media, respectively. The parameters $\epsilon^{(v)}$ and $\delta^{(v)}$ are the alternative Thomsen parameters used by Rüger (1998) to study HTI media. These terms are defined by Rüger (1998) as

$$
\begin{aligned}
\epsilon^{(v)} &= \frac{C_{11} - C_{33}}{2C_{33}} \equiv -\frac{\epsilon^r}{1 + 2\epsilon^r},\\
\delta^{(v)} &= \frac{(C_{13} + C_{66})^2 - (C_{33} - C_{66})^2}{2C_{33}(C_{33} - C_{66})}\\
&\equiv \frac{\delta^r - 2\epsilon^r(1 + \epsilon^r/f)}{(1 + 2\epsilon^r)(1 + 2\epsilon^r/f)}
\end{aligned}
\tag{A-2}
$$

where ϵ^r and δ^r are the Thomsen parameters defined in Thomsen (1995) rotated for an HTI coordinate system. The function f is defined as $f = 1 - v_{s_0}/v_{p_0}$, where v_{s_0} and v_{p_0} are the velocities perpendicular to fracturing. Rüger (1998) uses the same definition of γ as Thomsen (1995).

APPENDIX B

EFFEC MODELING

This appendix briefly outlines the effective flat fracture elastic compliance (EFFEC) approach used in the fractured medium modeling of the main text. This approach (from Hall, 2000) is based on the generalized theory described by Schoenberg and Sayers (1995), extended to allow quantification of the additional fracture compliance terms.

In general, a fracture can be considered as a poorly bonded interface that may have points of contact along its length and contains material that is different and, for the fractures of interest here, weaker in comparison to the surrounding media. Such fractures provide an additional compliance to a rock, which may be described by the excess fracture compliance tensor of Schoenberg and Sayers (1995), denoted Z_{ij}. Using this representation, Schoenberg and Sayers (1995) provide a general framework for determining the effective elastic compliance of a medium containing a number of aligned sets of low aspect-ratio fractures with arbitrary orientation. If the fractures are rotationally invariant about their normal axis and have no significant preferential slip direction, Z_{ij} may be simplified to include three nonzero elements given by just two independent terms, Z_N and Z_T, the normal and tangential fracture compliances:

$$
Z_{ij} = Z_N n_i n_j + Z_T(\delta_{ij} - n_i n_j), \tag{B-1}
$$

where δ_{ij} is the Kronecker delta and $\mathbf{n}$ is the fracture-normal vector. Thus, for such fractures Z_N and Z_T fully describe the additional compliance resulting from each fracture set and also represent the minimum amount of information that can be determined uniquely from seismic data.

One of the strengths of the Schoenberg and Sayers (1995) approach is its generality such that few assumptions need be made about the nature of aligned fracturing. However, this can also be a drawback. Thus, this general approach is extended (Hall, 2000) by drawing parallels with other fracture theories to create a hybrid scheme for describing the elasticity of fractures and fractured media. One of these extensions, and that used in this work, is the the so-called EFFECT approach, where the suffix "T" refers to the use of the work of Thomsen (1995) to define the additional fracture compliance terms. This approach includes hydraulic connectivity of fractures and pore space and is relevant for moderately high frequencies such that squirt flow has an influence on the fracture response but not so high that the timescale of the passage of a seismic wave is too short for fluid movement. In this model the excess compliances for penny-shaped cracks in a permeable matrix can be given as (Hall, 2000)

$$
Z_N = 2\epsilon^r\frac{(1 - \nu_b)^2}{1 - 2\nu_b}\frac{1}{\lambda_b + 2\mu_b}, \quad Z_T = \frac{2\gamma^r}{\mu_b}, \tag{B-2}
$$

where, for an HTI fractured medium,

$$\epsilon^r = \frac{C_{33} - C_{11}}{2C_{11}} = \left(\frac{8}{3}\right)\left(1 - \frac{K_f}{K_b}\right) D_{cp}\eta_c,$$
$$\gamma^r = \frac{C_{44} - C_{66}}{2C_{66}} = \left(\frac{8}{3}\right)\left(\frac{1 - \nu_b}{2 - \nu_b}\right)\eta_c \tag{B-3}$$

and ν_b is the Poisson's ratio of the solid matrix, while K_b and K_f are the bulk moduli of the solid matrix and the fracture material, respectively. With small amounts of equant porosity (<10%), the fluid influence parameter D_{cp} is (Thomsen, 1995)

$$D_{cp} = \left[1 - \frac{K_f}{K_b} + \frac{K_f}{K_b(\phi_p + \phi_c)}(A_p(\nu_b)\phi_p + A_c(\nu_b)\eta_c)\right]^{-1}, \tag{B-4}$$

where $\phi_c = (4/3)\eta_c \pi d$ is the fracture porosity (for crack density η_c and aspect ratio d), ϕ_p is the (equant) matrix porosity, $A_c(\nu_b) = [16(1 - \nu_b^2)]/[9(1 - 2\nu_b)]$ and $A_p(\nu_b) = [3(1 - \nu_b)]/[2(1 - 2\nu_b)]$.